

Metallicity of the Fossil Group NGC 1550 Observed with Suzaku

Kosuke SATO,¹ Madoka KAWAHARADA,² Kazuhiro NAKAZAWA,³
 Kyoko MATSUSHITA,⁴ Yoshitaka ISHISAKI,⁵ Noriko Y. YAMASAKI,² and Takaya OHASHI⁵

¹ *Kavli Institute for Astrophysics and Space Research, Massachusetts Institute of Technology,
 77 Massachusetts Ave., Cambridge, MA 02139, USA*

k_sato@mit.edu

³ *Institute of Space and Astronautical Science (ISAS), Japan Aerospace Exploration Agency,
 3-1-1 Yoshinodai, chuo-ku, Sagamihara, Kanagawa 252-5210*

³ *Department of Physics, University of Tokyo, 7-3-1 Hongo, Bunkyo, Tokyo 113-0033*

⁴ *Department of Physics, Tokyo University of Science, 1-3 Kagurazaka, Shinjuku-ku, Tokyo 162-8601*

⁵ *Department of Physics, Tokyo Metropolitan University, 1-1 Minami-Osawa, Hachioji, Tokyo 192-0397*

(Received 2010 August 11; accepted 2010 September 21)

Abstract

We studied the temperature and metal abundance distributions of the intra-cluster medium (ICM) in a group of galaxies NGC 1550 observed with Suzaku. The NGC 1550 is classified as a fossil group, which have few bright member galaxies except for the central galaxy. Thus, such a type of galaxy is important to investigate how the metals are enriched to the ICM. With the Suzaku XIS instruments, we directly measured not only Si, S, and Fe lines but also O and Mg lines and obtained those abundances to an outer region of $\sim 0.5 r_{180}$ for the first time, and confirmed that the metals in the ICM of such a fossil group are indeed extending to a large radius. We found steeper gradients for Mg, Si, S, and Fe abundances, while O showed almost flat abundance distribution. Abundance ratios of α -elements to Fe were similar to those of the other groups and poor clusters. We calculated the number ratio of type II to type Ia supernovae for the ICM enrichment to be 2.9 ± 0.5 within $0.1 r_{180}$, and the value was consistent with those for the other groups and poor clusters observed with Suzaku. We also calculated metal mass-to-light ratios (MLRs) for Fe, O and Mg with B-band and K-band luminosities of the member galaxies of NGC 1550. The derived MLRs were comparable to those of NGC 5044 group in the $r < 0.1 r_{180}$ region, while those of NGC 1550 are slightly higher than those of NGC 5044 in the outer region.

Key words: galaxies: groups: individual (NGC 1550), galaxies: intergalactic medium, galaxies: abundances

1. Introduction

Groups and clusters of galaxies play a key role for investigating the formation of the universe and they act as a building blocks in the framework of a hierarchical formation of structures. The metal abundances of Intra-cluster medium (ICM) in groups and clusters carry a lot of information in understanding the chemical history and evolution of groups and clusters. Recent X-ray observations allow us to measure temperature and metal abundance distributions in the ICM based on the spatially resolved spectra. A large amount of metals of the ICM are mainly produced by supernovae (SNe) in early-type galaxies (Arnaud et al. 1992; Renzini et al. 1993), which are classified roughly as type Ia (SNe Ia) and type II (SNe II). Because Si and Fe are both synthesized in SNe Ia and II, we need to know O and Mg abundances, which are synthesized predominantly in SNe II, in resolving the past metal enrichment process in ICM by supernovae. In order to know how the ICM has been enriched, we need to measure the amount and distribution of all the metals from O to Fe in the ICM.

Renzini (1997) and Makishima et al. (2001) summarized iron-mass-to-light ratios (IMLR) with B-band luminosity for various objects with ASCA, as a function of their plasma temperature serving as a measure of the system richness, and IMLRs in groups were found to be smaller than those in clusters. They also showed that the early-type galaxies released a large amount of metals which were probably formed through past supernovae explosions as shown earlier by Arnaud et al. (1992). In order to obtain a correct modeling of ICM, we need to know the correct temperature and metal abundance profiles without biases (e.g., Buote 2000; Sanders & Fabian 2002). Especially for the ICM of cooler systems, such as elliptical galaxies and groups of galaxies, careful analysis are required as mentioned in Arimoto et al. (1997) and Matsushita et al. (2000).

The spatial distribution and elemental abundance pattern of the ICM metals were determined with the large effective area of XMM-Newton (Matsushita et al. 2007b; Tamura et al. 2004; Böhringer et al. 2005; O’Sullivan et al. 2005; Sanders & Fabian 2006; de Plaa et al. 2006; de Plaa et al. 2007; Werner et al. 2006; Simionescu et al. 2008).

Table 1. Suzaku Observation logs for NGC 1550.

Region	Sequence No.	Observation date	(RA, Dec)* J2000.0	Exp. ksec	After screening (BI/FI) ksec
center	803017010	2008-08-16T04:27:05	(04 ^h 19 ^m 47 ^s .7, +02°24′38″)	83.3	82.0/83.3
offset	803018010	2008-08-15T02:44:04	(04 ^h 20 ^m 59 ^s .5, +02°24′31″)	41.1	40.5/40.7

* Average pointing direction of the XIS, written in the RA_NOM and DEC_NOM keywords of the event FITS files.

On the other hand, the abundance measurements of O and Mg with XMM-Newton were possible only for the central regions of brightest cooling core clusters due to the relatively high intrinsic background. Rasmussen & Ponman (2007); Rasmussen & Ponman (2009) report the Si and Fe profiles of 15 groups of galaxies observed with Chandra. They suggest that the Si to Fe ratios in groups tend to increase with radius, and the IMLRs within r_{500} show a positive correlation with total group mass (temperature). Suzaku XIS can measure all the main elements from O to Fe, because it realizes lower background level and higher spectral sensitivity, especially below 1 keV (Koyama et al. 2007). Suzaku observations have shown the abundance profiles of O, Mg, Si, S, and Fe to the outer regions with good precision for several clusters (Matsushita et al. 2007a; Sato et al. 2007a; Sato et al. 2008; Sato et al. 2009a; Sato et al. 2009b; Tokoi et al. 2008; Komiyama et al. 2009). Combining the Suzaku results with supernova nucleosynthesis models, Sato et al. (2007b) showed the number ratios of SNe II to Ia to be 3.5.

NGC 1550 is a S0 galaxy and one of the nearest ($z = 0.0124$) X-ray bright galaxies. The NGC 1550 is also classified as a fossil group (Jones et al. 2003), and an X-ray extended object RX J0419+0225 was first discovered by the ROSAT ALL SKY SURVEY from a position centered on the NGC 1550 galaxy. From ASCA observation (Kawaharada et al. 2003; Fukazawa et al. 2004), the MLRs with B-band is comparable to those of clusters. Sun et al. (2003) reports the temperature drop at the central region and also declines beyond 0.1 times of the virial radius, r_{180} , with Chandra observation. Kawaharada et al. (2009) shows the gas mass and metal mass from the temperature and metal abundances observed with XMM-Newton. In addition, they derived the mass-to-light ratios of O, Si, and Fe with near infrared (K-band) luminosity. The resultant IMLR within $\sim 200 h_{72}$ kpc exhibits about 2 orders of magnitude decrease toward the center. NGC 1550, such a fossil group, is a important object to investigate how the metals have been enriched to the ICM, because of little metal supply from the present-day member galaxies.

This paper reports on results from Suzaku observations of NGC 1550 out to $30' \simeq 457 h_{70}^{-1}$ kpc, corresponding to $\sim 0.47 r_{180}$. We use $H_0 = 70 \text{ km s}^{-1} \text{ Mpc}^{-1}$, $\Omega_{\Lambda} = 1 - \Omega_M = 0.73$ in this paper. At a redshift of $z = 0.0124$, $1'$ corresponds to 15.2 kpc, and the virial radius, $r_{180} = 1.95 h_{100}^{-1} \sqrt{k\langle T \rangle / 10 \text{ keV}} \text{ Mpc}$ (Markevitch et al. 1998), is 0.97 Mpc (63'.5) for an average temperature of $k\langle T \rangle = 1.2 \text{ keV}$. Throughout this paper we adopt the Galactic hydrogen column density of $N_{\text{H}} = 1.15 \times 10^{21} \text{ cm}^{-2}$ (Dickey & Lockman 1990) in the di-

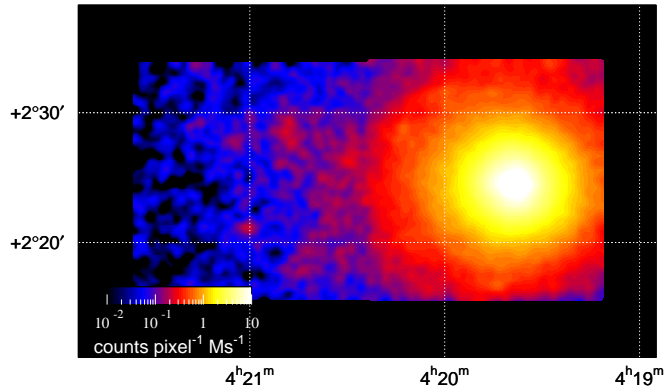


Fig. 1. Combined XIS image in the 0.5–2.0 keV energy range. The observed XIS0, 1, and 3 images were added on the sky coordinate after removing each calibration source region, and smoothed with $\sigma = 16 \text{ pixel} \simeq 17''$ Gaussian. Estimated components of extragalactic X-ray background (CXB) and instrumental background (NXB) were subtracted, and the exposure was corrected, though vignetting was not corrected. The white circles show the extracted regions in the spectral fits.

rection of NGC 1550. Unless noted otherwise, the solar abundance table is given by Anders & Grevesse (1989), and the errors are in the 90% confidence region for a single interesting parameter.

2. Observations and Data Reduction

2.1. Observations

Suzaku observed the central and offset regions of NGC 1550 in August 2008 (PI: K. Sato). The observation logs are given in table 1, and the XIS image in 0.5–2 keV is shown in figure 1. We analyzed only the XIS data in this paper, because the temperature of the HXD PIN is slightly higher during the observations. The XIS instrument consists of three sets of X-ray CCDs (XIS 0, 1, and 3). XIS 1 is a back-illuminated (BI) sensor, while XIS 0 and 3 are front-illuminated (FI). The instrument was operated in the normal clocking mode (8 s exposure per frame), with the standard 5×5 or 3×3 editing mode. During these observations, the significant effect of the Solar Wind Charge eXchange (SWCX) was not confirmed in ACE data ¹, although it was known that the SWCX affected the Suzaku spectra in the lower energy range as reported in Fujimoto et al. (2007) and Yoshino et al. (2009).

¹ <http://www.srl.caltech.edu/ACE/ASC>

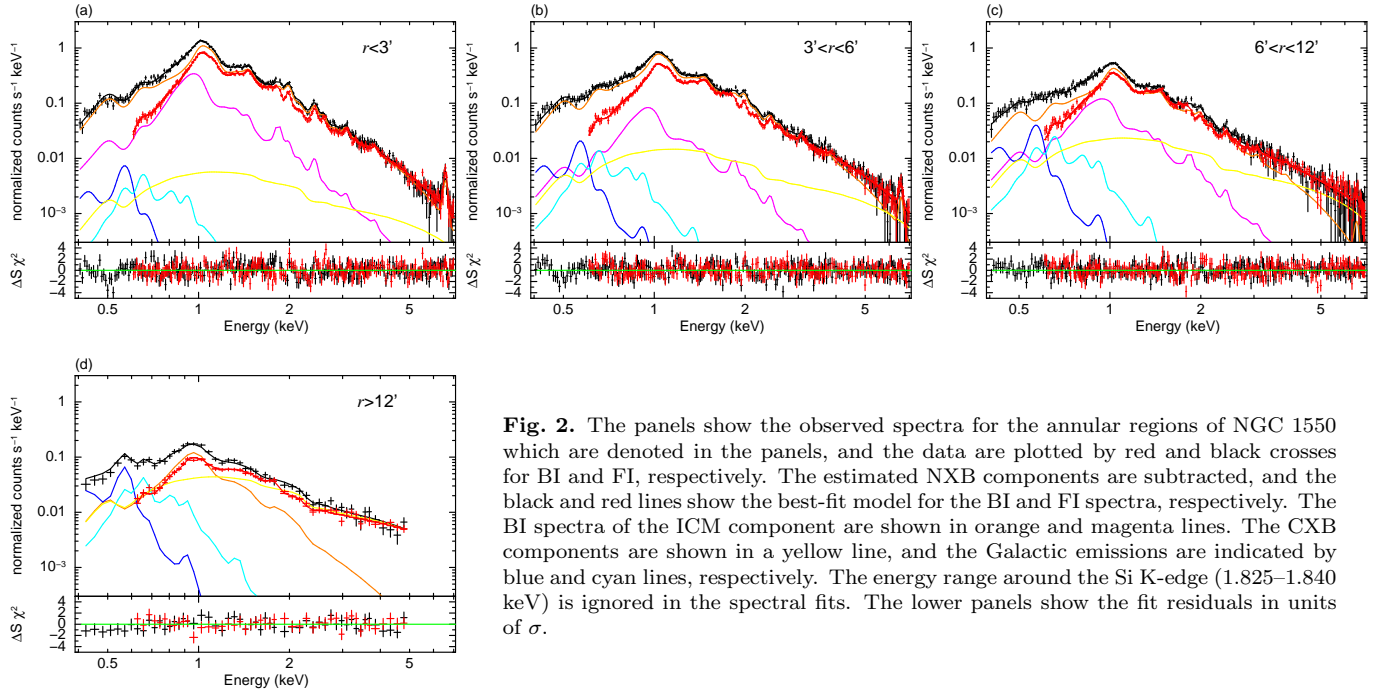


Fig. 2. The panels show the observed spectra for the annular regions of NGC 1550 which are denoted in the panels, and the data are plotted by red and black crosses for BI and FI, respectively. The estimated NXB components are subtracted, and the black and red lines show the best-fit model for the BI and FI spectra, respectively. The BI spectra of the ICM component are shown in orange and magenta lines. The CXB components are shown in a yellow line, and the Galactic emissions are indicated by blue and cyan lines, respectively. The energy range around the Si K-edge (1.825–1.840 keV) is ignored in the spectral fits. The lower panels show the fit residuals in units of σ .

2.2. Data Reduction

We used version 2.2 processing data, and the analysis was performed with HEASoft version 6.6.3 and XSPEC 12.5.0ac. Here we give just a brief description of the data reduction. The light curve of each sensor in the 0.3–10 keV range with a 16 s time bin was also examined in order to exclude periods with anomalous event rates which were greater or less than $\pm 3\sigma$ around the mean to remove the charge exchange contamination Fujimoto et al. (2007), while Suzaku data was little affected by the soft proton flare compared with XMM data. The exposure after the screening was essentially the same as that before screening in table 1, which indicated that the non X-ray background (NXB) was almost stable during the observation. Event screening with cut-off rigidity (COR) was not performed in our data. In order to subtract the NXB and the extra-galactic cosmic X-ray background (CXB), we employed the dark Earth database by the “xisnxbgen” Ftools task.

We generated two Ancillary Response Files (ARFs) for the spectrum of each annular sky region, A^U and A^B , which respectively assumed uniform sky emission and $\sim 1^\circ \times 1^\circ$ size of the β -model surface brightness profile, $\beta = 0.47$ and $r_c = 0'.85$, in Fukazawa et al. (2004), by the “xissimarfgen” Ftools task (Ishisaki et al. 2007). We also included the effect of the contaminations on the optical blocking filter of the XISs in the ARFs. Since the energy resolution also slowly degraded after the launch, due to radiation damage, this effect was included in the Redistribution Matrix File (RMF) by the “xisrmfgen” Ftools task.

3. Temperature and Abundance Profiles

3.1. Spectral Fit

We extracted spectra from five annular regions of $0'–3'$, $3'–6'$, and $6'–12'$ for the central observation, and whole area, which corresponds to $12'–30'$, for the offset region, centered on $(RA, Dec) = (4^h 19^m 37^s.9, +02^\circ 24' 36'')$. Each annular spectrum is shown in figure 2. The ionized Mg, Si, S, Fe lines are clearly seen in each region. The OVII and OVIII lines were prominent in the outer rings, however, most of the OVII line was considered to come from the local Galactic emission, and we dealt with those in the same way as mentioned in Sato et al. (2007a); Sato et al. (2008); Sato et al. (2009a); Sato et al. (2009b).

The spectra with BI and FI for all regions were fitted simultaneously in the energy range, 0.4–7.1/0.4–5.0 keV (BI) and 0.6–7.1/0.6–5.0 (FI) for the central/offset observations, respectively. In the simultaneous fit, the common Galactic emission and CXB components were included for all regions. We excluded the narrow energy band around the Si K-edge (1.825–1.840 keV) because its response was not modeled correctly. The energy range below 0.4 keV was also excluded because the C edge (0.284 keV) seen in the BI spectra could not be reproduced well in our data. The range above 7.1 keV was also ignored because Ni line (~ 7.5 keV) in the background left a spurious feature after the NXB subtraction at large radii. In the simultaneous fits of BI and FI data, only the normalization parameter was allowed to take different values between them.

It is important to estimate the Galactic component precisely, because the Galactic component gives significant contribution especially in the outer regions, as shown in figure 2. However, the ICM component is still dominant in almost all the energy range except for the OVII line. We assumed two temperature *apec* model (assuming 1 so-

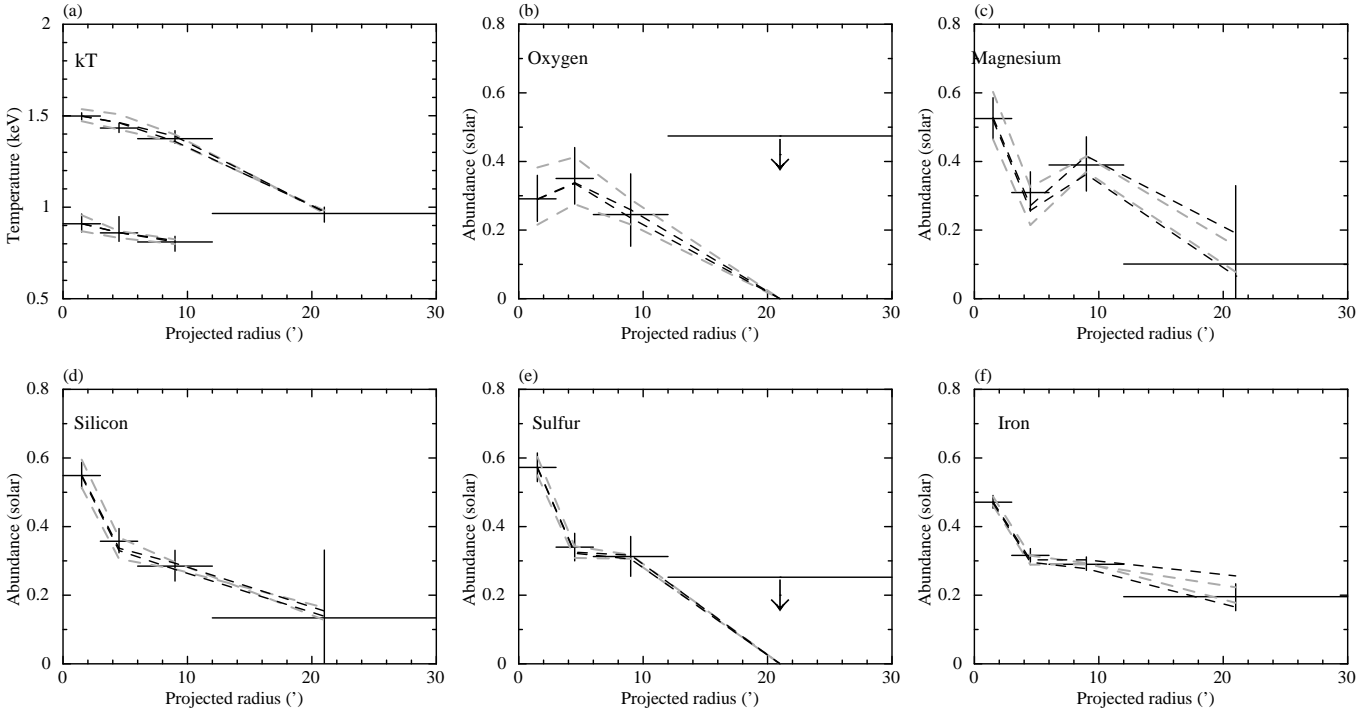


Fig. 3. (a): Radial temperature profiles derived from the spectral fits for each annulus against the projected radius. Black dashed lines show systematic change of the best-fit values by varying the thickness of the OBF contaminant by $\pm 10\%$. Light-gray dashed lines denote those when the NXB levels are varied by $\pm 10\%$. (b)–(f): Radial abundance profiles are plotted in the same way as in (a).

lar abundance and zero redshift) for the Galactic component, and fitted the data with the following model formula: $constant \times (apec_{cool} + phabs \times (apec_{hot} + ICM))$ as shown in Yoshino et al. (2009). As a result, the best-fit temperatures of 0.098 and 0.219 keV for the Galactic models as shown in table 2 are consistent with the values as shown in Yoshino et al. (2009) and Lumb et al. (2002). Thus, we concluded that the two temperature model of the Galactic emission was enough to represent NGC 1550 data. The resultant normalizations of the *apec* models in table 2 are scaled so that they give the surface brightness in unit solid angle of arcmin^2 , and are constrained to give the same surface brightness and the same temperature for the simultaneous fits of all annuli².

The ICM spectra for the central observation, $r < 12'$, were clearly better represented by two *vapex* models than one *vapex* model in the χ^2 test. On the other hand, the ICM spectra for the offset observation, $r = 12\text{--}30'$, were well-presented by a single temperature model. Thus, we carried out the simultaneous fit with the following formula of the Galactic and ICM components: $constant \times (apec_{cool} + phabs \times (apec_{hot} + vapex_{0 < r < 30'} + vapex_{0 < r < 12'}))$. The fit results are shown in table 2. The abundances were linked in the following way, $Mg=Al$, $S=Ar=Ca$, $Fe=Ni$, which gave good constraint especially for the offset regions. The abundances were also linked between the two *vapex* components for $r < 12'$ region. Results of the spectral fit for individual annuli are summarized in table 2

and figure 3, in which systematic error due to the OBF contamination and NXB estimation are shown.

3.2. Temperature Profile

Radial temperature profile and the ratio of the *vapex* normalizations between the hot and cool ICM components are shown in figure 3(a) and table 2. The ICM temperature of hot and cool components at the central region was ~ 1.5 and ~ 0.9 keV, respectively, and the temperature decreased mildly to ~ 1.0 keV in the outermost region, while the cool components were almost constant at ~ 0.9 keV. Our results for the two temperature ICM model are consistent with the XMM result (Kawaharada et al. 2009). For the hot component, our results are also consistent with the previous Chandra result (Sun et al. 2003). The radius of $30' \sim 457$ kpc corresponds to $\sim 0.47 r_{180}$, and the temperature decline is clearly recognized in such a small system out to this radius.

3.3. Abundance Profiles

Metal abundances are determined for the six element groups individually as shown in figures 3(b)–(f). The four abundance values for Mg, Si, S, and Fe and their radial variation look similar to each other. The central abundances lie around $\sim 0.5\text{--}0.6$ solar, and they commonly decline to about 1/4 of the central value in the outermost annulus. On the other hand, the O profile looks flatter compared with the other elements. Because the results for the offset regions had large errors, we examined the summed spectra for these regions. We noted that, when

² The Normalizations of “*norm*₁” in table 5 in Sato et al. (2008) are an order of magnitude larger than the actual values.

Table 2. Summary of the parameters of the fits to each annular spectrum of NGC 1550. All annuli were simultaneously fitted. Errors are 90% confidence range of statistical errors, and do not include systematic errors. The solar abundance ratio of *anqr* was assumed. These results are plotted in figure 3.

Galactic	$Norm_1^*$	kT_1 (keV)	$Norm_2^*$	kT_2 (keV)		
	$3.37^{+1.43}_{-1.14}$	$0.098^{+0.005}_{-0.014}$	$0.92^{+0.23}_{-0.58}$	$0.219^{+0.062}_{-0.046}$		
ICM	$Norm_1^\dagger$	kT_1 (keV)	$Norm_2^\dagger$	kT_2 (keV)	$Norm_1/Norm_2$	$\chi^2/\text{dof}^\ddagger$
0'-3'	$358.5^{+11.0}_{-6.1}$	$1.50^{+0.02}_{-0.02}$	$58.8^{+4.8}_{-4.7}$	$0.91^{+0.05}_{-0.05}$	$6.10^{+0.53}_{-0.49}$	613/463
3'-6'	$88.2^{+3.2}_{-1.8}$	$1.43^{+0.03}_{-0.02}$	$5.4^{+1.3}_{-0.9}$	$0.86^{+0.09}_{-0.05}$	$16.48^{+3.94}_{-2.89}$	531/469
6'-12'	$28.3^{+1.6}_{-0.9}$	$1.37^{+0.04}_{-0.03}$	$5.2^{+0.5}_{-2.8}$	$0.81^{+0.03}_{-0.05}$	$5.42^{+0.58}_{-2.96}$	520/469
12'-30'	$5.0^{+1.1}_{-0.6}$	$0.97^{+0.03}_{-0.05}$	—	—	—	73/91
total						1737/1492
ICM	O (solar)	Ne (solar)	Mg,Al (solar)	Si (solar)	S,Ar,Ca (solar)	Fe,Ni (solar)
0'-3'	$0.29^{+0.07}_{-0.07}$	$0.50^{+0.12}_{-0.12}$	$0.53^{+0.06}_{-0.06}$	$0.55^{+0.04}_{-0.04}$	$0.57^{+0.04}_{-0.04}$	$0.47^{+0.02}_{-0.02}$
3'-6'	$0.35^{+0.09}_{-0.07}$	$0.26^{+0.11}_{-0.10}$	$0.31^{+0.06}_{-0.05}$	$0.36^{+0.04}_{-0.03}$	$0.34^{+0.04}_{-0.04}$	$0.32^{+0.02}_{-0.02}$
6'-9'	$0.25^{+0.12}_{-0.09}$	$0.39^{+0.14}_{-0.14}$	$0.39^{+0.08}_{-0.08}$	$0.28^{+0.05}_{-0.04}$	$0.31^{+0.06}_{-0.06}$	$0.29^{+0.02}_{-0.02}$
9'-17'	$0.00^{+0.47}_{-0.00}$	$0.01^{+0.38}_{-0.01}$	$0.10^{+0.23}_{-0.10}$	$0.13^{+0.20}_{-0.13}$	$0.00^{+0.25}_{-0.00}$	$0.20^{+0.04}_{-0.04}$

* Normalization of the *apec* component divided by the solid angle, Ω^v , assumed in the uniform-sky ARF calculation (20' radius), $Norm = \int n_e n_H dV / (4\pi (1+z)^2 D_A^2) / \Omega^v \times 10^{-20} \text{ cm}^{-5} \text{ arcmin}^{-2}$, where D_A is the angular distance to the source.

† Normalization of the *vapex* component scaled with a factor of the selected region comparing to the assumed image in “xissimarfgen”, $Norm = factor \int n_e n_H dV / [4\pi (1+z)^2 D_A^2] \times 10^{-20} \text{ cm}^{-5} \text{ arcmin}^{-2}$, where D_A is the angular distance to the source.

‡ All regions were fitted simultaneously.

Table 3. List of χ^2/dof for the fits of the nominal and considering the systematic errors such as contaminant of OBF and background level. For details, see text.

Region	nominal	contaminant		background	
		+10%	-10%	+10%	-10%
All	1737/1492	1741/1492	1803/1492	1745/1492	1747/1492

we examined all abundances to be free in the fits, the resultant parameters did not change within the statistical errors. In addition, even if all regions were fitted by a two temperature model, the resultant abundance profiles did not change within the statistical errors.

We also examined the systematic error of our results by changing the background normalization by $\pm 10\%$, and the error range is plotted with light-gray dashed lines in figure 3. The systematic error due to the background estimation is almost negligible. The other systematic error concerning the uncertainty in the OBF contaminant is shown by black dashed lines as shown in figure 3. A list of χ^2/dof by changing the systematic errors is presented in table 3. We note that Ne abundance is not reliably determined due to an overlap with the strong and complex Fe-L line emissions, however we left these abundance to vary freely during the spectral fit.

4. Discussion

4.1. Metallicity Distribution in the ICM

Suzaku observation of NGC 1550 confirmed that the metals in the ICM of this fossil group are indeed extending to a large radius. The measured elements are O, Mg, Si, S, and Fe out to a radius of $30' \simeq 457 \text{ kpc}$, which corresponds to $\sim 0.47 r_{180}$, as shown in figure 3. The Ne abundance had a large uncertainty due to the strong coupling with Fe-L lines. Distributions of Mg, Si, S, and Fe are similar to each other, while O profile shows no central peak and large error in the outer region at $r > 12'$. We plotted abundance ratios of O, Mg, Si, and S to Fe as a function of the projected radius in figure 4. The ratios Mg/Fe, Si/Fe and S/Fe are consistent to be a constant value around 1.5–2, while O/Fe ratio in the innermost region ($r < 3'$) is significantly lower around 0.5. In addition, the O/Fe ratio suggests some increase with radius. Note that these abundance profiles are not deconvolved and are averaged over the line of sight.

Recent Suzaku observations have presented abundance

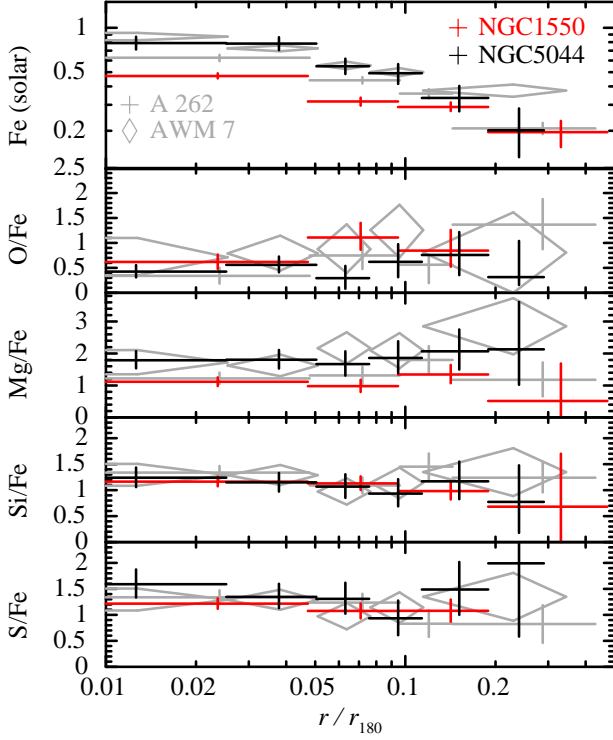


Fig. 4. Comparison of the Fe abundance and the other metals to the Fe abundance ratios for NGC 1550 (red crosses) with those for the NGC 5044 group (black crosses; Komiyama et al. 2009), A 262 cluster (light gray crosses; Sato et al. 2009b) and AWM 7 cluster (light gray diamonds; Sato et al. 2008). The Fe abundance and the O/Fe, Mg/Fe, Si/Fe, and S/Fe abundance ratios in solar units (Anders & Grevesse 1989) are plotted against the projected radius scaled by the virial radius, r_{180} , in all panels.

profiles in several relaxed cooling core groups and clusters: a group of galaxies NGC 5044 (Komiyama et al. 2009), a poor cluster of galaxies Abell 262 (Sato et al. 2009b), and AWM 7 (Sato et al. 2008). We compare Fe abundance and O, Mg, Si, S to Fe abundance ratios of NGC 1550 with those of NGC 5044, Abell 262 and AWM 7 as shown in figure 4. While NGC 1550 shows slightly lower Fe abundance than those of NGC 5044, Abell 262, and AWM 7 in the central region ($r \lesssim 0.1 r_{180}$), the abundance in the outer region ($r \gtrsim 0.3 r_{180}$) are quite similar, showing a decrease to ~ 0.2 solar. On the other hand, the abundance ratios of O/Fe, Mg/Fe, Si/Fe, and S/Fe are quite similar between the four systems.

Matsushita (2010) reports the Fe radial profiles of 28 clusters of galaxies observed with XMM. The Fe abundance profile of NGC 1550 also has similar feature to those of clusters up to $\sim 0.5 r_{180}$. Although Rasmussen & Ponman (2009) suggests that the radial Si profiles in group have softer than the Fe profiles, our results show the constant values of the Si to Fe ratios up to $\sim 0.5 r_{180}$ as shown in figure 4.

4.2. Number Ratio of SNe II to SNe Ia

In order to examine relative contributions from SNe Ia and SNe II to the ICM metals, the elemental abundance

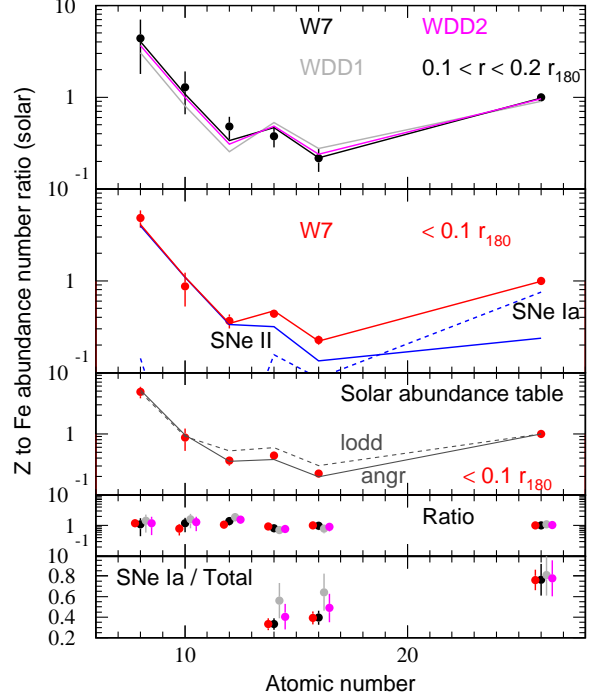


Fig. 5. Fit results of number ratios of elements to Fe of NGC 1550. Top and second panel show the abundance number ratios in solar unit in $0.1 < r < 0.2 r_{180}$ (black) and $0.1 < r < 0.2 r_{180}$ (red) regions, respectively. Blue dashed and solid lines in the second panel correspond to the contributions of SNe Ia (W7) and SNe II within $0.1 r_{180}$, respectively. Ne (atomic number = 10) is excluded in the fit. Third panel shows the comparison with solar abundance table of Anders & Grevesse (1989) (light-gray line) and Lodders (2003) (dashed light-gray line). Forth panel indicates ratios of data points to the best-fit model. Bottom panel indicates fractions of the SNe Ia contribution to total metals in the best-fit model for each element, respectively.

pattern of O, Mg, Si, S and Fe was examined for the inner ($r < 0.1 r_{180}$) and the immediate outer ($0.1-0.2 r_{180}$) regions. The abundance ratios to Fe were fitted by a combination of average SNe Ia and SNe II yields per supernova, as shown in figure 5. The fit parameters were the integrated number of SNe Ia (N_{Ia}) and the number ratio of SNe II to SNe Ia ($N_{\text{II}}/N_{\text{Ia}}$), because N_{Ia} could be well constrained by the relatively small errors in the Fe abundance. The SNe Ia and II yields were taken from Iwamoto et al. (1999) and Nomoto et al. (2006), respectively. We assumed the Salpeter IMF for stellar masses from 10 to $50 M_{\odot}$ with the progenitor metallicity of $Z = 0.02$ for SNe II, and W7, WDD1 or WDD2 models for SNe Ia. Table 4 and figure 5 summarize the fit results. The number ratios were better represented by the W7 SNe Ia yield model than by WDD1. The number ratio of SNe II to SNe Ia with W7 is ~ 2.9 within $0.1 r_{180}$, while the ratio assuming WDD1 is ~ 2.1 . The WDD2 model gave the result very similar to the W7 value. The resultant number ratios are consistent with the previous result by Sato et al. (2007b). We also compared the abundance pattern of NGC 1550 with the solar abundance. The third panel in figure 5 shows this

Table 4. Integrated number of SNe I (N_{Ia}) and number ratio of SNe II to SNe Ia ($N_{\text{II}}/N_{\text{Ia}}$).

Region	SNe Ia Model	N_{Ia}	$N_{\text{II}}/N_{\text{Ia}}$	χ^2/dof
$< 0.1 r_{180}$	W7	$1.3 \pm 0.1 \times 10^8$	2.9 ± 0.5	3.7/3
$0.1 - 0.2 r_{180}$	W7	$2.6 \pm 0.4 \times 10^8$	2.8 ± 1.0	5.7/3
$< 0.1 r_{180}$	WDD1	$1.3 \pm 0.1 \times 10^8$	2.1 ± 0.5	44.2/3
$0.1 - 0.2 r_{180}$	WDD1	$2.8 \pm 0.5 \times 10^8$	2.0 ± 1.0	21.0/3
$< 0.1 r_{180}$	WDD2	$1.2 \pm 0.1 \times 10^8$	2.8 ± 0.6	10.4/3
$0.1 - 0.2 r_{180}$	WDD2	$2.4 \pm 0.4 \times 10^8$	2.8 ± 1.1	8.9/3

comparison for $r < 0.1 r_{180}$ of NGC 1550 with two different solar abundance patterns given by Anders & Grevesse (1989) and Lodders (2003). Abundances of Mg, Si, and S fall between the two solar abundance patterns.

Almost $\sim 80\%$ of Fe and $\sim 40\%$ of Si and S were synthesized by SNe Ia in the W7 model, as demonstrated in the bottom panel of figure 5. These observed features of the fossil group are similar to those for clusters with $kT = 2 - 4$ keV clusters studied by Sato et al. (2007b) and Sato et al. (2009b). The values in table 4 imply that the $N_{\text{II}}/N_{\text{Ia}}$ ratio for the inner and outer regions behave in the similar manner for different supernova models. We note that the fit was not formally acceptable based on the χ^2 value in table 4. As described in Sato et al. (2007b), the models adapted here (SNe yield, Salpeter IMF, etc.) are probably too simplified.

4.3. Metal Mass-to-Light Ratio

We derived 3-dimensional gas mass profile by extending the previous XMM-Newton result (Kawaharada et al. 2009) for the region within $14'$ arcmin ($\sim 0.2 r_{180}$). Combining it with the abundance profiles obtained with Suzaku, we calculated cumulative metal mass. The derived masses of Fe and Mg within the 3-dimensional radius of $r < 457$ kpc ($r \sim 0.5 r_{180}$) are 1.3×10^9 , $3.4 \times 10^8 M_{\odot}$, respectively, and the O mass within $r < 183$ kpc is $1.7 \times 10^9 M_{\odot}$. Errors of the metal mass, which were used to calculate mass-to-light ratios, were taken from the statistical errors of each elemental abundance in the spectral fits, because these are much larger than the error of gas mass by Kawaharada et al. (2009).

We examined mass-to-light ratios for O, Fe, and Mg (OMLR, IMLR, and MMLR, respectively) which enabled us to compare the ICM metal distribution with the stellar mass profile. Historically, B-band luminosity has been used for the estimation of the stellar mass (Makishima et al. 2001), however we calculated it using the K-band luminosity in NGC 1550 based on the Two Micron All Sky Survey (2MASS) catalogue³. This method is useful in performing a uniform comparison with the properties in other groups and clusters based on the same K-band galaxy catalogue to trace the distribution of member elliptical galaxies.

In the 2MASS catalog, we used all the data in a $2^\circ \times 2^\circ$ region around NGC 1550 without the selection of galaxy morphology, and subtracted the luminosity in a $r > 1^\circ$ re-

gion, which corresponds to about r_{180} , as the background. We then deprojected the luminosity profile as a function of radius assuming a spherical symmetry. In order to convert the K-band magnitude of each galaxy to the B-band value, we assumed the luminosity distance $D_L = 53.6$ Mpc, and an appropriate color $B - K = 4.2$ for early-type galaxies given by Lin & Mohr (2004), along with the Galactic extinction $A_B = 0.583$ from NASA/IPAC Extragalactic Database (NED) in the direction of NGC 1550.

The integrated values of OMLR, IMLR, and MMLR using the estimated B-band luminosity within $r \lesssim 183$ kpc ($r \lesssim 0.2 r_{180}$) turned out to be $\sim 3.3 \times 10^{-2}$, $\sim 7.4 \times 10^{-3}$, and $\sim 3.3 \times 10^{-3} M_{\odot}/L_{B\odot}$, respectively, as shown in table 5. The errors are based only on the statistical errors of metal abundance in the spectral fit, and the uncertainties in the gas mass profile and the luminosities of member galaxies are not included. Note that we did not adjust metal-mass and K-band profiles by considering the Suzaku PSF effect, because uncertainties in the metal mass had the dominant effect in our MLR estimation.

We compared these B-band MLRs for NGC 1550 with those of other groups and clusters. The MLRs are all measured within inner ($\sim 0.1 r_{180}$) and outer ($\sim 0.25 r_{180}$) regions as shown in table 5 and figure 6. As for Fe (IMLR), NGC 1550 shows a similar value with the other groups and poor clusters in the inner region. As mentioned in subsection 4.1, the Fe abundance itself of NGC 1550 in the inner region is slightly smaller than those in other groups and clusters. However, the IMLR in this region is almost the same as others, due to somewhat low value of stellar mass in NGC 1550. Looking at the outer region, NGC 1550 shows slightly higher IMLR than NGC 5044 and comparable to those in other poor clusters. On the other hand for the OMLR in the inner region, the poor systems show much lower values than the larger high-temperature systems. Interestingly, the poor systems (including NGC 1550) show higher OMLR in the outer region, comparable to those in the larger systems. The spatial extent of O looks to be relatively large in these very small systems.

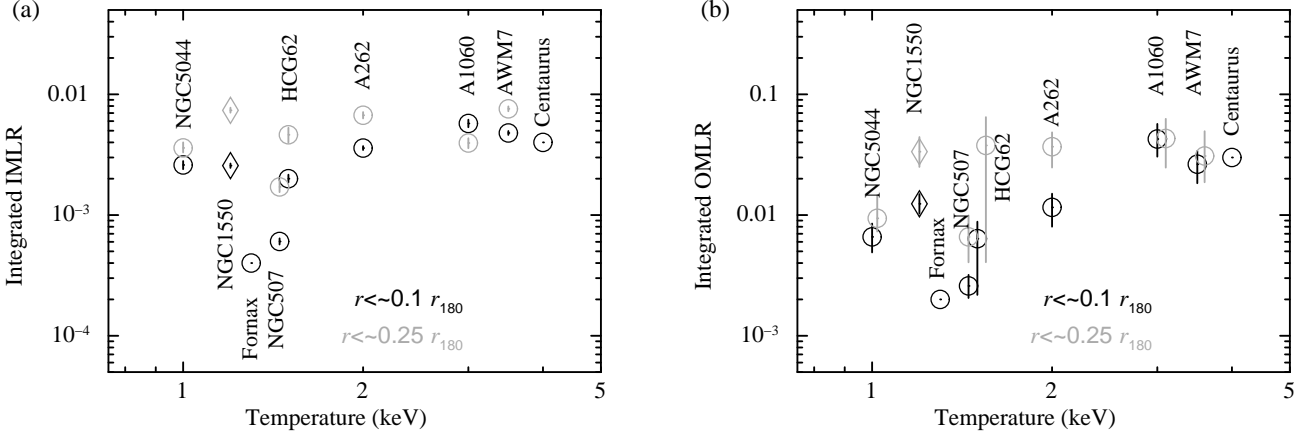
Rasmussen & Ponman (2009) suggests that the IMLRs within r_{500} of 15 groups of galaxies observed with Chandra have a positive correlation with the groups mass (temperature). Our results and Chandra's results are also almost consistent, and the IMLRs of groups are slightly lower than those of clusters.

We also calculated the MLRs by directly using the K-

³ The database address: <http://www.ipac.caltech.edu/2mass/>

Table 5. Comparison of IMLR, OMLR and MMLR with B-band luminosity for all systems.

	IMLR (M_{\odot}/L_{\odot}^B)	OMLR (M_{\odot}/L_{\odot}^B)	MMLR (M_{\odot}/L_{\odot}^B)	r (kpc)	r (r_{180})	$k\langle T \rangle$ (keV)	Reference
Suzaku							
NGC 5044 ...	$2.6^{+0.2}_{-0.2} \times 10^{-3}$	$6.6^{+1.9}_{-1.7} \times 10^{-3}$	$1.6^{+0.2}_{-0.2} \times 10^{-3}$	88	0.10	~ 1.0	Komiyama et al. (2009)
	$3.6^{+0.4}_{-0.3} \times 10^{-3}$	$9.4^{+5.2}_{-2.1} \times 10^{-3}$	$2.6^{+0.4}_{-0.3} \times 10^{-3}$	260	0.30		
NGC 1550 ...	$2.6^{+0.1}_{-0.1} \times 10^{-3}$	$1.2^{+0.3}_{-0.2} \times 10^{-3}$	$9.4^{+1.2}_{-1.1} \times 10^{-4}$	46	0.09	~ 1.2	This work
	$7.4^{+0.4}_{-0.4} \times 10^{-3}$	$3.3^{+1.1}_{-0.8} \times 10^{-2}$	$3.3^{+0.5}_{-0.5} \times 10^{-3}$	183	0.19		
Fornax	4×10^{-4}	2×10^{-3}	—	130	0.13	~ 1.3	Matsushita et al. (2007b)
NGC 507	$6.0^{+0.4}_{-0.3} \times 10^{-4}$	$2.6^{+0.6}_{-0.5} \times 10^{-3}$	$3.7^{+0.4}_{-0.4} \times 10^{-4}$	120	0.11	~ 1.5	Sato et al. (2009a)
	$1.7^{+0.2}_{-0.2} \times 10^{-3}$	$6.6^{+3.3}_{-2.5} \times 10^{-3}$	$1.1^{+0.2}_{-0.2} \times 10^{-3}$	260	0.24		
HCG 62	$2.0^{+0.1}_{-0.1} \times 10^{-3}$	$6.4^{+0.2}_{-0.4} \times 10^{-3}$	$1.0^{+0.2}_{-0.1} \times 10^{-3}$	120	0.11	~ 1.5	Tokoi et al. (2008)
	$4.6^{+0.7}_{-0.6} \times 10^{-3}$	$3.8^{+2.7}_{-3.4} \times 10^{-2}$	$1.5^{+0.4}_{-0.4} \times 10^{-3}$	230	0.21		
A 262	$3.6^{+0.1}_{-0.1} \times 10^{-3}$	$1.2^{+0.3}_{-0.4} \times 10^{-2}$	$1.6^{+0.2}_{-0.2} \times 10^{-3}$	130	0.10	~ 2	Sato et al. (2009b)
	$6.7^{+0.4}_{-0.4} \times 10^{-3}$	$3.7^{+1.2}_{-1.2} \times 10^{-2}$	$2.7^{+0.7}_{-0.6} \times 10^{-3}$	340	0.27		
A 1060	$5.7^{+0.2}_{-0.4} \times 10^{-3}$	$4.3^{+0.8}_{-0.8} \times 10^{-2}$	$2.4^{+0.5}_{-0.5} \times 10^{-3}$	180	0.12	~ 3	Sato et al. (2007a)
	$4.0^{+0.4}_{-0.4} \times 10^{-3}$	$4.3^{+2.0}_{-1.8} \times 10^{-2}$	$1.6^{+0.8}_{-0.7} \times 10^{-3}$	380	0.25		
AWM 7	$4.8^{+0.2}_{-0.2} \times 10^{-3}$	$2.6^{+0.8}_{-0.8} \times 10^{-2}$	$3.4^{+0.5}_{-0.5} \times 10^{-3}$	180	0.11	~ 3.5	Sato et al. (2008)
	$7.6^{+0.4}_{-0.3} \times 10^{-3}$	$3.1^{+1.9}_{-1.2} \times 10^{-2}$	$6.7^{+1.1}_{-1.1} \times 10^{-3}$	360	0.22		
XMM-Newton							
Centaurus ...	4×10^{-3}	3×10^{-2}	—	190	0.11	~ 4	Matsushita et al. (2007a)

**Fig. 6.** Comparison of IMLR (a) and OMLR (b) with B-band luminosity to the other clusters and groups within $\sim 0.1 r_{180}$ (black) and $\sim 0.25 r_{180}$ (light gray) region. The MLRs of NGC 1550 are shown by the diamonds.**Table 6.** Integrated mass-to-light ratios of O, Mg, and Fe (OMLR, MMLR, IMLR) with K-band luminosity in units of M_{\odot}/L_{\odot}^K .

Region (kpc/ r_{180})	OMLR	MMLR	IMLR
$<45.7/0.05$	$9.4^{+2.2}_{-2.1} \times 10^{-4}$	$1.1^{+0.1}_{-0.1} \times 10^{-4}$	$2.9^{+0.1}_{-0.1} \times 10^{-4}$
$<91.3/0.09$	$3.5^{+0.7}_{-0.6} \times 10^{-3}$	$2.6^{+0.3}_{-0.3} \times 10^{-4}$	$7.1^{+0.3}_{-0.3} \times 10^{-4}$
$<182.6/0.19$	$9.2^{+0.3}_{-0.3} \times 10^{-3}$	$9.0^{+1.4}_{-1.3} \times 10^{-4}$	$2.0^{+0.1}_{-0.1} \times 10^{-3}$
$<456.6/0.47$	—	$9.0^{+1.0}_{-4.5} \times 10^{-4}$	$3.5^{+0.5}_{-0.5} \times 10^{-3}$

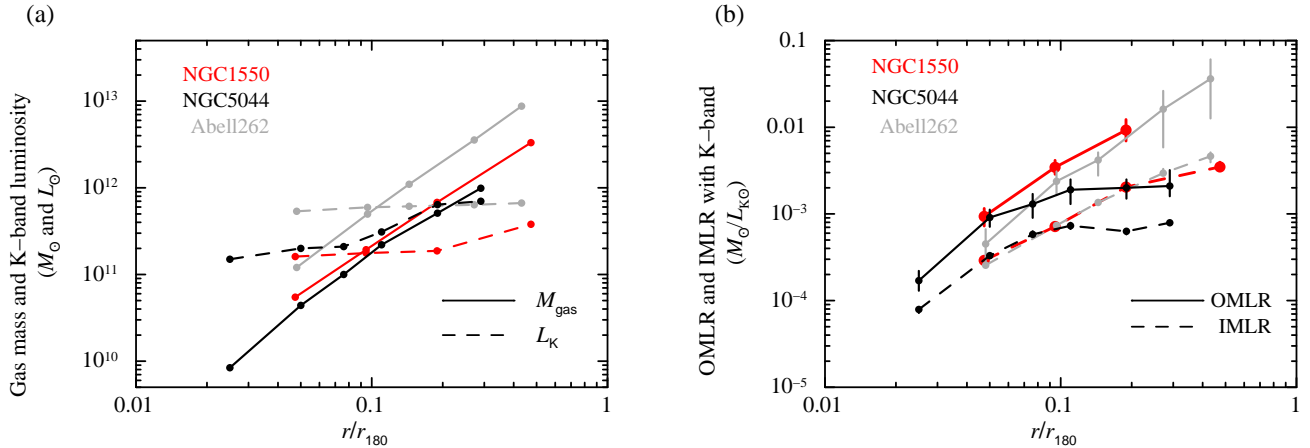


Fig. 7. (a) Gas mass, $M(< R)$, and K-band luminosity, L_K within the 3-dimensional radius, R , in NGC 1550, NGC 5044, and Abell 262. The gas mass profiles derived from XMM-Newton observations for NGC 1550 (Kawaharada et al. 2009), NGC 5044 (Komiya et al. 2009), and Abell 262 (Gastaldello et al. 2007). The red, black, and light-gray lines show each value for NGC 1550, NGC 5044, and Abell 262, respectively. The solid and dashed lines corresponds to each gas mass and K-band luminosity, respectively. (b) Ratios of the O and Fe mass in units of M_{\odot} to the K band luminosity in units of L_{\odot} (OMLR and IMLR, respectively) for NGC 1550, NGC 5044, and Abell 262, against the 3-dimensional radius. The solid and dashed lines corresponds to each OMLR and IMLR, respectively.

band luminosity assuming the Galactic extinction $A_K = 0.050$ in the direction of NGC 1550, and the absolute K-band solar magnitude of 3.34. The resultant K-band luminosity within the Suzaku observed region, $r < 30'$, is $3.8 \times 10^{11} L_{K\odot}$, and the radial luminosity profile is also plotted in figure 7(a). We calculated the radial profile of the OMLR, IMLR, and MMLR values using the K-band luminosity out to a radius $r \sim 180$ kpc ($r \lesssim 0.2 r_{180}$), as shown in figure 7(b) and table 6. The values at the outermost radius are $\sim 9.2 \times 10^{-3}$, $\sim 2.0 \times 10^{-3}$, and $\sim 9.0 \times 10^{-4} M_{\odot}/L_{K\odot}$, respectively.

In order to investigate the dependence on the system size, we compared the MLRs of NGC 1550 ($kT \approx 1.2$ keV) with those of NGC 5044 (1 keV) and Abell 262 (2 keV), which are all poor relaxed cooling-core groups and clusters. Although they show similar IMLR in the inner region, NGC 1550 and Abell 262 show gas mass ratio to the K-band luminosity higher than NGC 5044, as shown in figure 7(a). As one goes outside ($r > 0.1 r_{180}$), NGC 1550 shows fairly consistent MLRs with Abell 262, larger than those in NGC 5044 as shown in figure 6(b). The radial profiles of IMLR and OMLR for NGC 1550 look quite similar to those for Abell 262 rather than for NGC 5044.

The radius, $r \sim 0.1 r_{180}$, corresponds to the region where the gas mass and K-band luminosity seem to overlap as shown in figure 7(a). Assuming the stellar mass-to-light ratio, $M_{\text{star}}/L_K \sim 1$ as shown in Arnouts et al. (2007) (see also Nagino & Matsushita 2009), this radius indeed corresponds to the point where the gas and stellar masses are comparable. The similarity of MLRs for the 3 systems examined here in the inner region ($r < 0.1 r_{180}$) suggests that the metal enrichment within the past few Gyr has occurred in a similar way. On the other hand, in the outer region ($r > 0.1 r_{180}$), NGC 5044 shows lower IMLR than those in NGC 1550 and Abell 262, even though Fe abundances themselves are comparable in these regions.

This suggests that distribution of stellar mass has some different history between these systems.

We will consider how the observed features of abundance and MLR profiles can constrain enrichment scenario. First, metals in the inner region ($r \lesssim 0.1 r_{180}$) have been mostly supplied by the central galaxy, so this region should be set aside in the present discussion. In the immediate outer region ($r \gtrsim 0.1 r_{180}$), metals from the central galaxy could not reach in a few Gyr time scale. Also, we may assume that almost the same amount of metals per stellar mass was synthesized in all systems before the collapse of groups and clusters. In this case, we expect very similar MLRs in different systems, contrary to the observed feature. As shown in figure 7(b), at least NGC 5044 shows lower IMLR and OMLR profiles compared with those for two other systems. This implies that the thermal and/or dynamical evolutions of the gas have different history among different systems during or after the collapsing period of individual groups and clusters.

Renzini (2005) showed the expected MLRs as a function of the IMF slope. As for OMLR, the expected value to be $\sim 0.1 M_{\odot}/L_B$ at a Salpeter IMF is slightly higher than our results of $\sim 0.03 M_{\odot}/L_B$ within $\sim 0.25 r_{180}$ as shown in figure 6(b). However, as shown in figure 7(b), because the OMLRs look increasing toward outer region, the OMLRs within the virial radius would be represented with the Salpeter IMF. Renzini (2005) also suggested that a top heavy IMF would overproduce metals by more than a factor of 20, which is much larger than the observed values including our results.

We stress that high-sensitivity abundance observation to the outer region of clusters will give important clues about their evolution. If O distribution, as well as Fe, could be measured to the very outer region ($r \sim r_{180}$), we may obtain a clear view about when O and Fe were supplied to the inter galactic space because most of O

should have been synthesized by SNe II and supplied in the starburst era. Another possibility is very early metal enrichment of O by galaxies or massive Population III stars (e.g. Matteucci et al. 2006) before groups and clusters assemble. In this case, a large part of the intergalactic space would be enriched quite uniformly with O and other elements. Metallicity information in cluster outskirts would thus give us unique information about the enrichment history. For this purpose, instruments with much higher energy resolution, such as microcalorimeters, and optics with larger effective area will play a key role in carrying out these studies.

5. Summary and conclusion

Suzaku observation of the fossil group NGC 1550 showed spatial distributions of temperature and metal abundances for O, Mg, Si, S, and Fe up to $\sim 0.5 r_{180}$ for the first time, and confirmed that the metals in the ICM of this fossil group are indeed extending to a large radius. The ICM temperature decreases mildly from ~ 1.5 keV to ~ 1.0 keV in the outer region, similar to the feature seen in other clusters. The abundances of Mg, Si, S, and Fe drop from subsolar levels at the center to $\sim 1/4$ solar in the outermost region, while the O abundance shows a flatter distribution around ~ 0.5 solar without the strong concentration in the center. The abundance ratios, O/Fe, Mg/Fe, Si/Fe, and S/Fe for NGC 1550 are generally similar to those in groups and poor clusters. The abundance pattern from O to Fe enabled us to constrain number ratio of SNe II to Ia as 2.9 ± 0.5 , which is consistent with the values obtained for other groups and clusters. The derived MLRs of NGC 1550 using the B-band and K-band luminosities are consistent with those in the NGC 5044 group for the inner region $r \lesssim 0.1 r_{180}$, while NGC 1550 shows slightly higher MLRs than NGC 5044 in the outer region. This suggests that metal enrichment process may reflect the size of the system in the sense that larger systems contain higher amount of metals for a given stellar mass.

Authors thank the referee for providing valuable comments. K.S is supported by a JSPS Postdoctoral fellowship for research abroad. Part of this work was financially supported by the Ministry of Education, Culture, Sports, Science and Technology, Grant-in-Aid for Scientific Research Nos. 20340068, 21224003, 21740134.

References

- Anders, E., & Grevesse, N. 1989, *Geochim. Cosmochim. Acta*, 53, 197
- Arimoto, N., Matsushita, K., Ishimaru, Y., Ohashi, T., & Renzini, A. 1997, *ApJ*, 477, 128
- Arnaud, M., Rothenflug, R., Boulade, O., Vigroux, L., & Vangioni-Flam, E. 1992, *A&A*, 254, 49
- Arnouts, S., et al. 2007, *A&A*, 476, 137
- Böhringer, H., Matsushita, K., Finoguenov, A., Xue, Y., & Churazov, E. 2005, *Advances in Space Research*, 36, 677
- Buote, D. A. 2000, *MNRAS*, 311, 176
- Buote, D. A., Brighenti, F., & Mathews, W. G. 2004, *ApJL*, 607, L91
- de Plaa, J., Werner, N., Bleeker, J. A. M., Vink, J., Kaastra, J. S., & Méndez, M. 2007, *A&A*, 465, 345
- de Plaa, J., et al. 2006, *A&A*, 452, 397
- Dickey, J. M., & Lockman, F. J. 1990, *ARA&A*, 28, 215
- Fujimoto, R., et al. 2007, *PASJ*, 59, 133
- Fukazawa, Y., Makishima, K., & Ohashi, T. 2004, *PASJ*, 56, 965
- Gastaldello, F., Buote, D. A., Humphrey, P. J., Zappacosta, L., Bullock, J. S., Brighenti, F., & Mathews, W. G. 2007, *ApJ*, 669, 158
- Ishisaki, Y., et al. 2007, *PASJ*, 59, 113
- Iwamoto, K., Brachwitz, F., Nomoto, K., Kishimoto, N., Umeda, H., Hix, W. R., & Thielemann, F.-K. 1999, *ApJS*, 125, 439
- Jones, L. R., Ponman, T. J., Horton, A., Babul, A., Ebeling, H., & Burke, D. J. 2003, *MNRAS*, 343, 627
- Kawaharada, M., Makishima, K., Kitaguchi, T., Okuyama, S., Nakazawa, K., & Fukazawa, Y. 2009, arXiv:0911.5205
- Kawaharada, M., Makishima, K., Takahashi, I., Nakazawa, K., Matsushita, K., Shimasaku, K., Fukazawa, Y., & Xu, H. 2003, *PASJ*, 55, 573
- Komiyama, M., Sato, K., Nagino, R., Ohashi, T., & Matsushita, K. 2009, *PASJ*, 61, 337
- Koyama, K., et al. 2007, *PASJ*, 59, 23
- Lin, Y.-T., & Mohr, J. J. 2004, *ApJ*, 617, 879
- Lodders, K. 2003, *ApJ*, 591, 1220
- Lumb, D. H., Warwick, R. S., Page, M., & De Luca, A. 2002, *A&A*, 389, 93
- Makishima, K., et al. 2001, *PASJ*, 53, 401
- Markevitch, M., et al. 1998, *ApJ*, 503, 77
- Matsushita, K., Ohashi, T., & Makishima, K. 2000, *PASJ*, 52, 685
- Matsushita, K., Finoguenov, A., Böhringer, H. 2003, *A&A*, 401, 443
- Matsushita, K., Böhringer, H., Takahashi, I., & Ikebe, Y. 2007b, *A&A*, 462, 953
- Matsushita, K., et al. 2007a, *PASJ*, 59, 327
- Matsushita, K. submitted to *A&A*
- Matteucci, F., Panagia, N., Pipino, A., Mannucci, F., Recchi, S., & Della Valle, M. 2006, *MNRAS*, 372, 265
- Nagino, R., & Matsushita, K. 2009, *A&A*, 501, 157
- Nomoto, K., Tominaga, N., Umeda, H., Kobayashi, C., & Maeda, K. 2006, *Nuclear Physics A*, 777, 424
- O’Sullivan, E., Vrtillek, J. M., Kempner, J. C., David, L. P., & Houck, J. C. 2005, *MNRAS*, 357, 1134
- Rasmussen, J., & Ponman, T. J. 2009, *MNRAS*, 399, 239
- Rasmussen, J., & Ponman, T. J. 2007, *MNRAS*, 380, 1554
- Renzini, A., Ciotti, L., D’Ercole, A., & Pellegrini, S. 1993, *ApJ*, 419, 52
- Renzini, A. 1997, *ApJ*, 488, 35
- Renzini, A. 2005, *The Initial Mass Function 50 Years Later*, 327, 221
- Sanders, J. S., & Fabian, A. C. 2002, *MNRAS*, 331, 273
- Sanders, J. S., & Fabian, A. C. 2006, *MNRAS*, 371, 1483
- Simionescu, A., Werner, N., Finoguenov, A., Böhringer, H., & Brüggen, M. 2008, *A&A*, 482, 97
- Sato, K., et al. 2007a, *PASJ*, 59, 299
- Sato, K., Tokoi, K., Matsushita, K., Ishisaki, Y., Yamasaki, N. Y., Ishida, M., & Ohashi, T. 2007, *ApJL*, 667, L41
- Sato, K., Matsushita, K., Ishisaki, Y., Yamasaki, N. Y., Ishida, M., Sasaki, S., & Ohashi, T. 2008, *PASJ*, 60, S333

- Sato, K., Matsushita, K., Ishisaki, Y., Yamasaki, N. Y., Ishida, M., & Ohashi, T. 2009a, PASJ, 61, 353
- Sato, K., Matsushita, K., & Gastaldello, F. 2009b, PASJ, 61, 365
- Sun, M., Forman, W., Vikhlinin, A., Hornstrup, A., Jones, C., & Murray, S. S. 2003, ApJ, 598, 250
- Tamura, T., Kaastra, J. S., Makishima, K., & Takahashi, I. 2003, A&A, 399, 497
- Tamura, T., Kaastra, J. S., den Herder, J. W. A., Bleeker, J. A. M., & Peterson, J. R. 2004, A&A, 420, 135
- Tawara, Y., et al. 2008, PASJ, 60, S307
- Tokoi, K., et al. 2008, PASJ, 60, S317
- Werner, N., de Plaa, J., Kaastra, J. S., Vink, J., Bleeker, J. A. M., Tamura, T., Peterson, J. R., & Verbunt, F. 2006a, A&A, 449, 475
- Yoshino, T., et al. 2009, PASJ, 61, 805